The International Journal of Advanced Manufacturing Technology (2023) 128:3471–3489
https://doi.org/10.1007/s00170-023-12155-w

ORIGINAL ARTICLE

Effects of printing parameters on the mechanical characteristics and mathematical modeling of FDM-printed PETG

Rajan Kumaresan[1] · Mahendran Samykano[1,2] · Kumaran Kadirgama[1,2] · Adarsh Kumar Pandey[3,4] · Md. Mustafizur Rahman[1]

Received: 25 January 2023 / Accepted: 13 August 2023 / Published online: 21 August 2023
© The Author(s), under exclusive licence to Springer-Verlag London Ltd., part of Springer Nature 2023

Abstract

3D printing technology has revolutionized free-form construction and customization demand through its ease of use, fast production, accurate, regulated deposition, and flexibility with soft functional materials. Fused deposition modeling (FDM) is an ideal technique for the 3D printing of plastics. The low cost, high prototyping precision, and ease of use make it a popular additive manufacturing process. The dimensional stability, quality, functionality, and properties of printed specimens are all affected by the process parameters used in the FDM technology. As such, the present work investigates the effect of the infill pattern and infill density on the PETG mechanical characteristics. The work also finds the optimum parameters to enhance the mechanical properties using the response surface methodology (RSM). Scanning electron microscopy (SEM) was used to study micro-surface defects under different processing conditions. Based on the tensile strength experiments, the concentric pattern was recorded to have the highest UTS, *E*, and yield values compared to the other designs, at 28.53 MPa, 0.81 GPa, and 20.00 MPa, respectively. In contrast, from compression analysis, the highest compression strength and compression modulus (24.03 MPa and 3.71 GPa, respectively) were obtained for the triangular infill pattern, which absorbs more compressive force compared with the other patterns. Meanwhile, it was also observed that increasing the density from 25 to 75% improves mechanical properties. The RSM analysis reveals the significant parameters for both testing methodologies with mathematical models to predict the properties with 95% certainty.

Keywords Fused deposition modeling · Polyethylene terephthalate glycol · Mechanical characteristics · Response surface methodology · ANOVA · Scanning electron microscopy

Highlights • Effect of various infill patterns and infill percentages on the tensile properties.

• Effect of various infill patterns and infill percentages on the compressive properties.

• Microstructural analysis is performed to analyze the failure mechanism.

• Optimization of process variables to achieve a desired maximum or minimum response value.

✉ Mahendran Samykano
mahendran@ump.edu.my

1 Faculty of Mechanical & Automotive Engineering Technology, Universiti Malaysia Pahang Al-Sultan Abdullah, 26600 Pekan, Pahang, Malaysia

2 Centre for Research in Advanced Fluid and Processes, Universiti Malaysia Pahang Al-Sultan Abdullah, 26300 Gambang, Pahang, Malaysia

3 Research Centre for Nano-Materials and Energy Technology (RCNMET), School of Science and Technology, Sunway University, No. 5, Jalan Universiti, Bandar Sunway, 47500 Petaling Jaya, Selangor Darul Ehsan, Malaysia

4 CoE for Energy and Eco-Sustainability Research, Uttaranchal University, Dehradun, Uttarakhand 248007, India

1 Introduction

Global demand for new and customized products has been increasing in recent years. In order to meet the request, the quickest way to create working prototypes of products designed using computer-aided design (CAD) is by using additive manufacturing (AM) [1] techniques. The

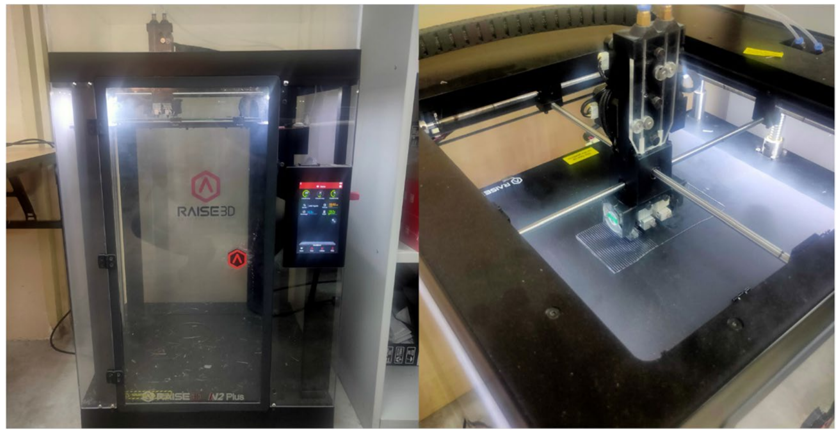

Fig. 1 Raise 3D N2 plus printer setup

term "layered manufacturing" describes the process by which things are joined together in a staggered series of layers. AM is a process where the model is built using CAD data by depositing material in precise geometric layers [2]. In contrast to conventional methods, additive manufacturing does not necessitate a secondary finishing stage like machining. Several additive manufacturing has been developed, each distinguished by a unique set of materials and technologies for constructing successive layers of the product. In the beginning, AM was employed in the manufacturing and industrial sectors to build visual representations of products. As a result of developments in AM, the functional product or individual components can be manufactured and utilized as final products [3]. AM has contributed significantly in the fields of aircraft, medicine, the food industry, and the automotive sector. Additionally, research scholars have been using this method to create analytical and research models for various research activities. Compared to conventional manufacturing methods, AM's time and cost savings, minimal equipment, and simple manufacturing process have been their primary advantages [4, 5].

Additive manufacturing (AM) techniques can be broken down into three broad categories based on the materials used: liquid, solid, and powder [6–8]. Material extrusion (ME), vat photopolymerization (VP), sheet lamination (SL), powder bed fusion (PBF), binder jetting (BJ), material jetting (MJ), and directed energy deposition (DED) are all good examples of AM processes [9]. Fused deposition modeling (FDM) technology has become the most popular additive manufacturing approach due to its low production costs and user-friendliness. The FDM technique adapts the layer-by-layer melt-extrusion of a plastic filament to form three-dimensional structures [10]. The fabrication of the structure began with the generation of a digital design of the model by 3D design software, followed by the printer's execution of that design until the entire model was printed [11]. FDM was developed by Stratasys co-founder Scott Crump in 1989 and is currently the most widely used additive manufacturing technique based on material extrusion. FDM's promising future is evidenced by its numerous advancements and successful applications in recent years [12]. FDM was employed as an alternative production process to make PPE during the COVID-19 epidemic, specifically face masks and respirator face shields. Between 2020 and 2021, many FDM-optimized materials have been created [13]. FDM is an extrusion method that uses thermoplastic polymers such as acrylonitrile butadiene styrene (ABS), polylactic acid

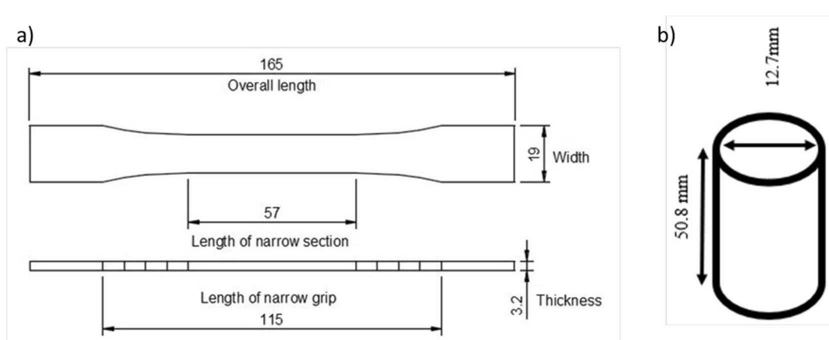

Fig. 2 **a** ASTM D638 type-I standard for tensile samples. **b** ASTM D695 standard for compression samples

Table 1 Build parameters for the tensile and compressive ASTM standards

Printing parameters	Standards
Initial layer thickness	0.30 mm
Layer height	0.20 mm
Solid layer	Bottom: 7-layer, top: 5-layer
Filament diameter	1.75 mm (±0.05 mm)
Extruder temperature	240 °C (±2 °C)
Print bed temperature	75 °C (±2 °C)
Printing speed	30 mm/min
Raster angle	0°

Table 2 Mechanical properties of polyethylene terephthalate glycol (PETG)

Properties	Testing sample type	Typical value
Young's modulus	ASTM D638	1.48 ± 0.27 (GPa)
Tensile strength		31.9 ± 1.1 (MPa)
Elongation at break		6.8 ± 0.9 (MPa)
Compressive strength	ASTRM D695	21.08 ± 1.3 (MPa)
Compressive modulus		3.02 ± 0.2 (GPa)

(PLA), and polycarbonate (PC). Polyetherimide (PEI) are typically employed in the production of final products, including device housing and other functional prototypes [14, 15]. Selecting suitable printing parameters during fabrication is crucial for the exceptional performance of FDM products. The precision of the variable and the material qualities vary as a result of the availability of several competing parameters. The effectiveness and mechanical qualities of the fabricated product may be traced back to the process parameters that were used. The primary parameters for FDM printing are the air gap, build orientation, layer thickness, infill pattern, infill density, operating temperature, raster width, angle, and printing speed [13]. Out of this, the critical design factors were interlayer bonding, layer thickness, infill pattern, and raster angle. However, FDM's major hurdles in creating operational or functional parts are inconsistent surfaces, inferior mechanical qualities, and a lack of precision [16, 17].

Polyethylene terephthalate glycol (PETG) has a greater level of popularity due to its strength, relative flexibility, and excellent thermal stability advantages. PETG is typically simpler to work with and has the advantage of being safe for food applications [18, 19]. In addition, PETG is also recyclable material, adding advantage towards waste minimization and environmental effects. PETG can also be formed in a vacuum or heated to a high temperature without cracking, making it versatile. PETG's inherent transparency makes it suitable for esthetic applications [20, 21]. Researchers Hanon et al. [18] investigated the effects of infill density, build orientation, and raster angle on the tensile properties of PETG and concluded that 0° raster angle achieves good strength. The impact of airgap on the mechanical properties of PETG was analyzed by Özen et al. [13], and their findings reveal that reducing the air gap between the layer increases the bonding of the layers and enhances the product's strength. Srinivasan et al. [22] investigated the impact properties of the PETG part by varying the infill patterns. The raster angle was kept constant at 0° for all 8 infill patterns. The grid pattern was reported to have optimum impact properties. The parameter effect on the surface roughness (R_a) was analyzed by Barrios and Romero [23], and they concluded that reducing the layer thickness and printing speed will be helpful to achieve a good surface finish. Hsueh et al. [24] analyzed the effect of printing temperature (215 to 235 °C) and printing speed (30–50 mm/s) on PLA and PETG parts by using FDM. Their results show that increasing the printing temperature helps to increase the strength, and increasing the speed reduces the print quality and strength of the product. Guessasma et al. [21] examined the impact of nozzle temperatures between 210 and 250 °C on PETG's tensile strength and discovered that the material warped on the platform until PETG filament was printed at a

Fig. 3 FDM-printed tensile and compression samples per ASTM standards

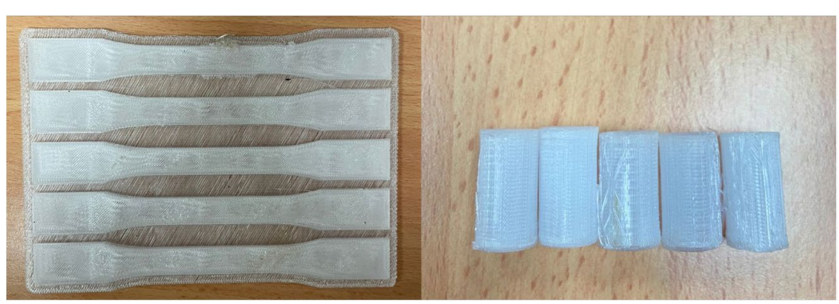

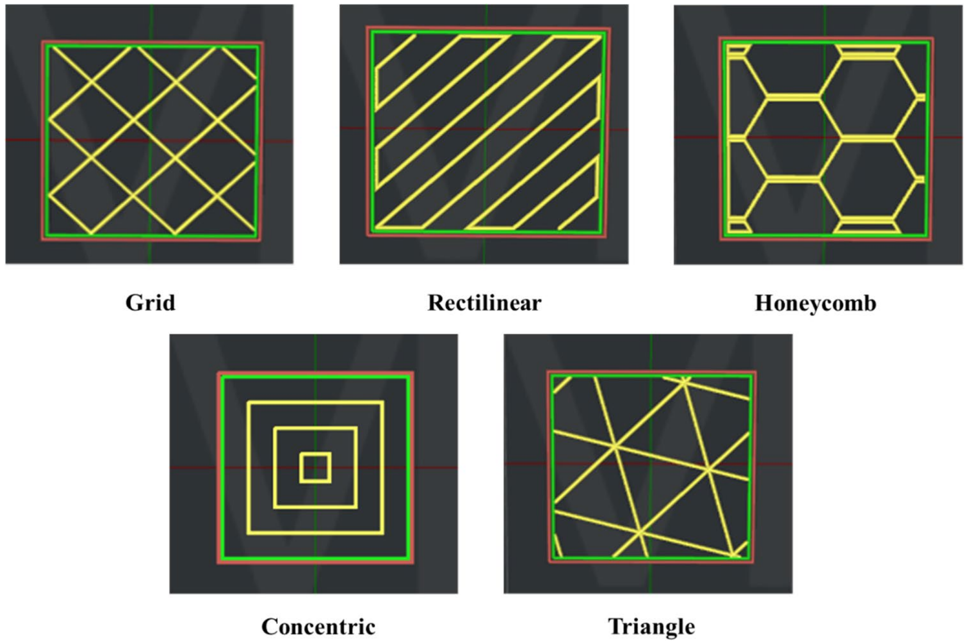

Fig. 4 Various infill patterns

temperature of at least 230 °C. Maximum porosity of 2% and average roughness of around 100 μm are achieved at a nozzle temperature of 250 °C.

In terms of research prospects, most studies have only analyzed the association between FDM process parameters and test specimens' mechanical behavior. It is crucial to know the suitable parameters to achieve optimum mechanical properties. Thus, in this research, the tensile and compressive properties of the PETG at various parameters such as infill density (25%, 50%, and 75%) and infill pattern (grid, honeycomb, rectilinear, concentric, and triangle) are investigated. The optimal FDM parameters to enhance the product strength are identified using the response surface methodology (RSM) technique. RSM optimizes complex findings using empirical statistical modeling. The findings from the present work are expected to provide insights into the parameters' effect towards the mechanical behavior of the PETG. Our research suggests that PETG would be ideal for FDM manufacturing applications.

Table 3 Average tensile properties of FDM-printed PETG

Sl.No	Infill pattern	Infill percentage	UTS (MPa)	*E* (GPa)	Yield (0.2% offset)
1	Grid	25%	18.45	0.32	10.59
2	Rectilinear		17.42	0.30	10.13
3	Honeycomb		18.10	0.31	10.48
4	Concentric		19.25	0.35	11.49
5	Triangle		14.58	0.28	7.64
6	Grid	50%	24.28	0.47	15.68
7	Rectilinear		23.18	0.51	14.54
8	Honeycomb		24.27	0.52	15.24
9	Concentric		25.85	0.57	16.98
10	Triangle		19.75	0.46	11.93
11	Grid	75%	27.26	0.61	19.95
12	Rectilinear		26.98	0.70	19.54
13	Honeycomb		27.10	0.71	19.74
14	Concentric		28.53	0.81	20.00
15	Triangle		22.16	0.59	17.02

2 Methodology

The Raise 3D N2 plus, an FDM-type 3D printer, was used to produce the test specimens shown in Fig. 1. The polylite™ enterprise supplies the 1.75 ± 0.05 mm PETG transparent filament, which is a polymer that is based on polyester. The tensile and compression tests were created following the ASTM standards provided in Fig. 2, which are ASTM D638 type-I and ASTM D695 samples, respectively. The parameters of the process, specifically the infill density and the infill pattern, were altered, while all of the other parameters, including layer thickness, raster angle, etc., were fixed. Table 1 summarizes the parameters together with their corresponding units of measure. Table 2 provides the mechanical properties of the PETG specimens with 100% infill density (tensile and compressive). According to ASTM standards, the test samples were designed using the Solidworks CAD software and transferred to Ideamaker. Ideamaker is the

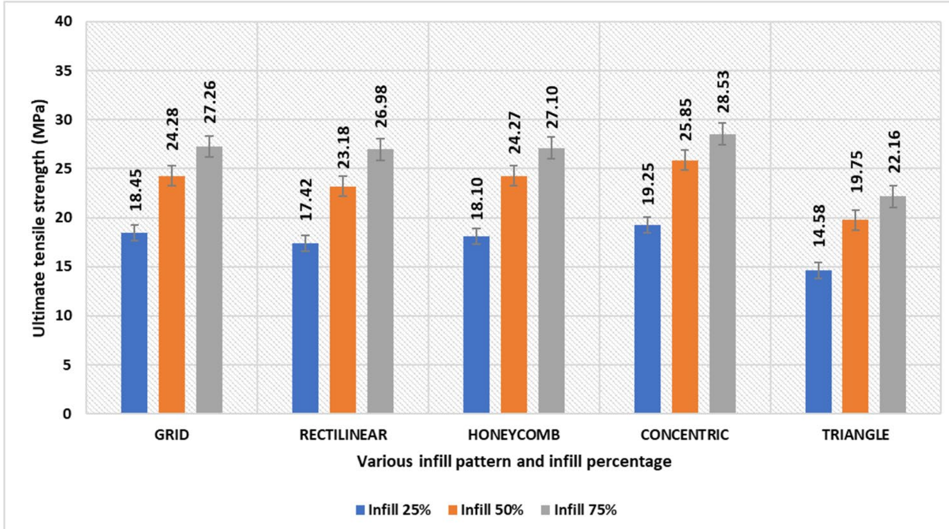

Fig. 5 Average UTS value of PETG with various infill patterns and infill percentages

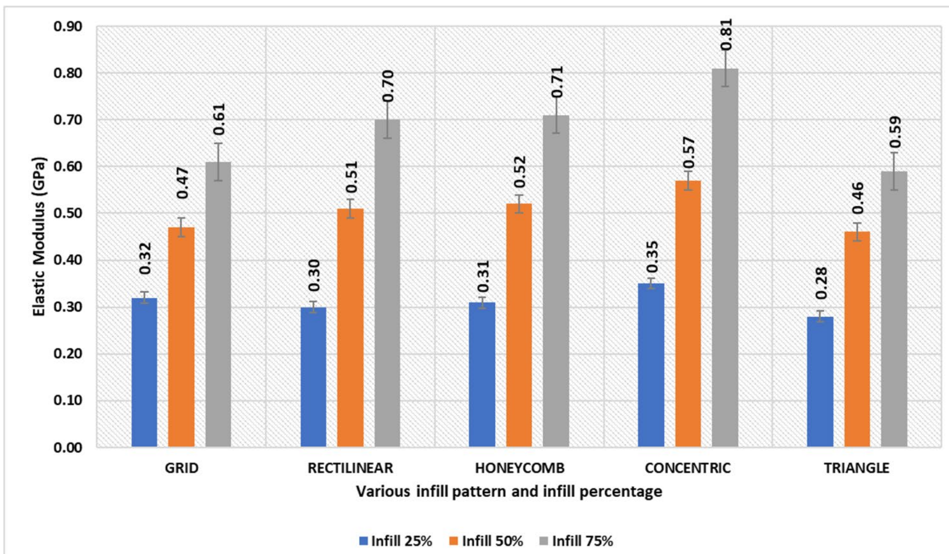

Fig. 6 Average elastic modulus value of PETG with various infill patterns and infill percentages

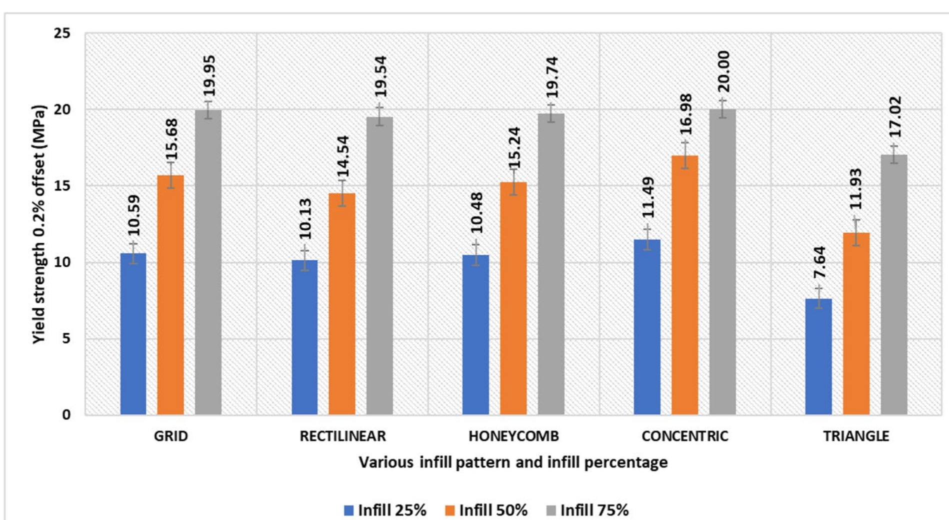

Fig. 7 Average yield value of PETG with various infill patterns and infill percentages

Table 4 Average compressive properties of FDM-printed PETG

Sl.No	Infill pattern	Infill percentage	Compressive strength (MPa)	Compressive modulus (GPa)
1	Grid	25%	11.29	1.54
2	Rectilinear		10.54	1.45
3	Honeycomb		10.68	1.50
4	Concentric		8.15	0.89
5	Triangle		12.57	1.63
6	Grid	50%	17.45	2.89
7	Rectilinear		16.84	2.56
8	Honeycomb		16.89	2.67
9	Concentric		13.54	1.54
10	Triangle		18.23	2.92
11	Grid	75%	21.84	3.54
12	Rectilinear		22.36	3.49
13	Honeycomb		22.48	3.51
14	Concentric		18.97	2.74
15	Triangle		24.03	3.71

slicing software that helps control the process parameters and creates the G-codes for the printing process of the specimens. For each variation, $n = 5$ samples were printed and a total of 75 samples each for the tensile and compression prepared. Figure 3 shows the FDM-printed tensile and compression test specimens according to ASTM standards. Instron 3367 is used to conduct the tensile testing with the capacity of 30 kN and Instron 2501 series is used for the compression test with the capacity of 600 kN. SEM analysis was carried out using Hitachi TM3030 Plus tabletop microscope to analyze the microstructure and bonding of the layers. Finally, the RSM technique is used for optimization and to find suitable parameters for optimum behavior. The applicable range of the regression equations is limited as per the build parameters in Table 1. Figure 4 demonstrates the various infill patterns used in this study.

3 Results and discussion

3.1 Tensile properties

The amount of load or stress that a material is able to withstand before it begins to stretch and break is referred to as its tensile strength. The resistance of a material to the tension created by mechanical loads being applied to the material is referred to as its tensile strength, which is self-explanatory, given its name. One essential characteristic of materials used for structural purposes is their capacity to withstand breaking when subjected to tensile stress. This property is also one of the most commonly measured. The measured average tensile properties of the PETG are shown in Table 3 for various compositions.

3.1.1 Ultimate tensile strength

The ultimate tensile strength (UTS) is the amount of stress a material can sustain while being pulled or stretched to its breaking point before it gives way. Figure 5 displays the obtained

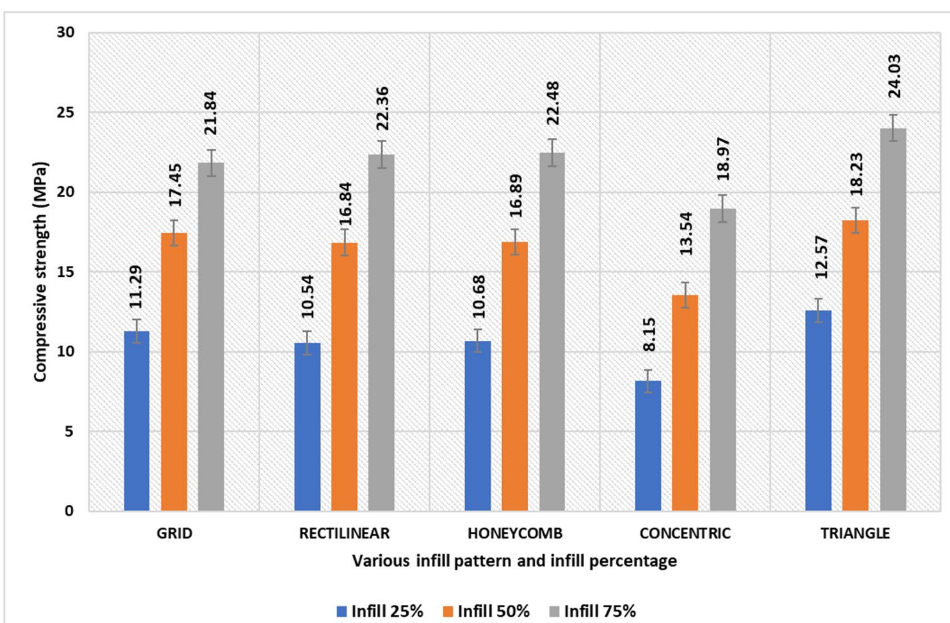

Fig. 8 Average compressive strength value of PETG with various infill patterns and infill percentages

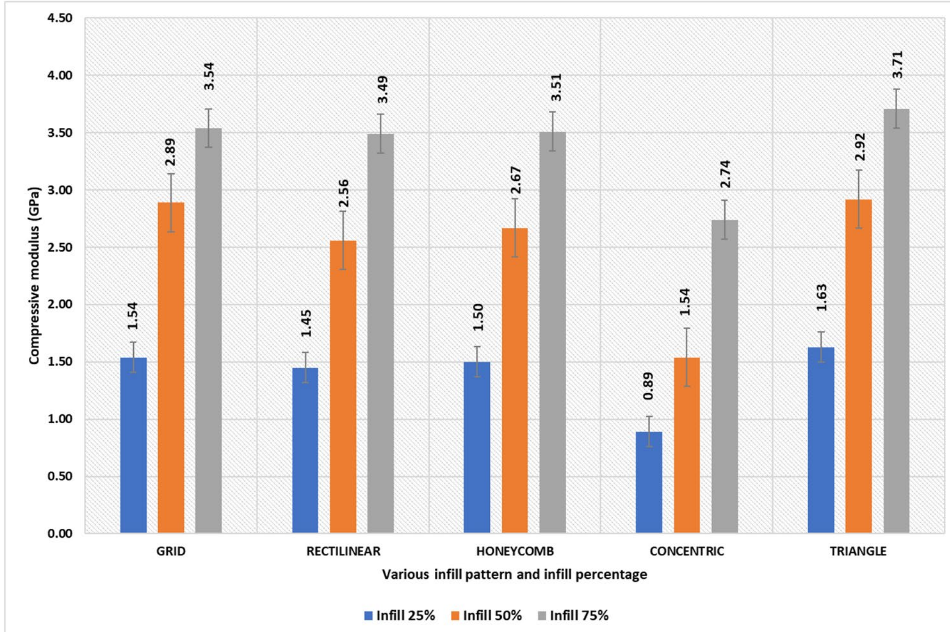

Fig. 9 Average compressive modulus value of PETG with various infill patterns and infill percentages

average UTS properties by the PETG with various infill patterns and infill percentages. Findings showed that the best performance characteristics were attained at 75% infill density, while the lowest characteristics were achieved at 25% infill density. According to the findings, the highest UTS value of 28.53 MPa was attained by the concentric infill pattern with an infill density of 75%. The lowest value obtained was 14.58 MPa for a triangle infill pattern with 25% infill density. With respect to the other infill patterns (grid, honeycomb, rectilinear, and triangle), the concentric obtained the highest strength at 28.53 MPa.

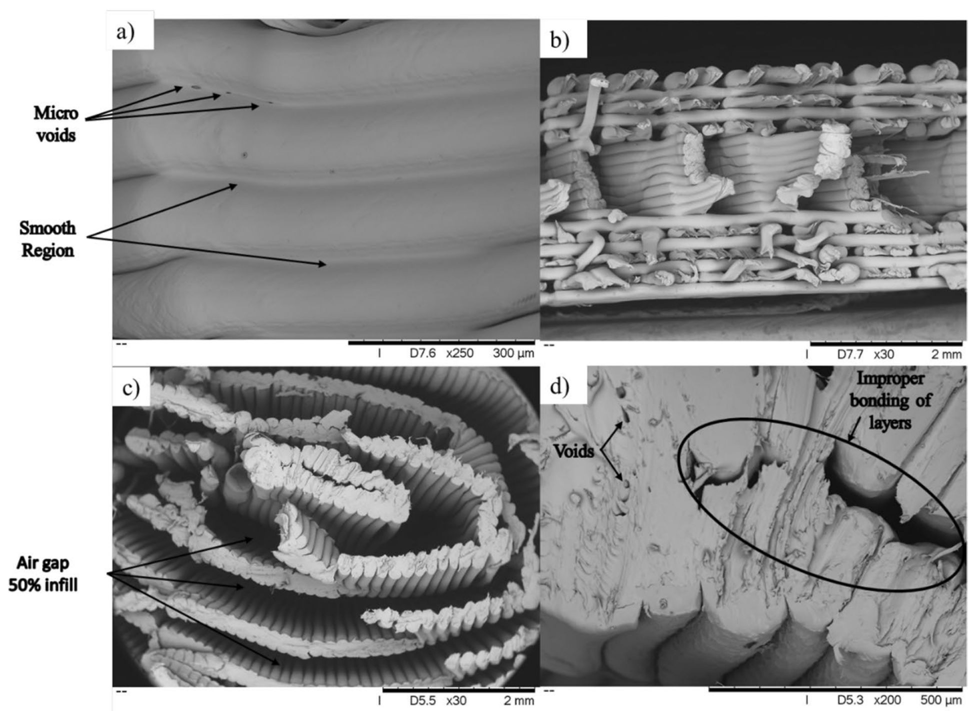

Fig. 10 The microstructure of FDM-printed PETG standards under varying conditions of processing as shown by SEM

Table 5 Analysis of variance of UTS

Source	DF	Contribution	Adj SS	Adj MS	*F* value	*P* value
Model	10	99.86%	260.410	26.041	295.09	0.000
Linear	5	96.61%	251.916	50.383	570.94	0.000
Infill %	1	75.02%	195.629	195.629	2216.85	0.000
Infill pattern	4	21.59%	56.287	14.072	159.46	0.000
Square	1	2.81%	7.331	7.331	83.07	0.001
Infill %*Infill %	1	2.81%	7.331	7.331	83.07	0.001
2-Way interaction	4	0.45%	1.163	0.291	3.29	0.137
Infill %*Inf. pattern	4	0.45%	1.163	0.291	3.29	0.137
Error	4	0.14%	0.353	0.088		
Total	14	100.00%				
$R^2 = 99.86\%$						
R^2 adjusted = 99.53%						
R^2 predicted = 97.14%						

3.1.2 Elastic modulus

The stiffness of a material is described by its elastic modulus (E), which is one of the most important properties of solids. It is the relationship between the stress and the strain of a material. Stress is force per unit area, while strain is lengthening or shortening per unit length. Figure 6 shows the maximum E value of 0.81 GPa obtained at the concentric infill pattern with 75% infill density. The triangle infill pattern with 25% infill density gave the lowest value of E, which was 0.28 GPa. Similarly, the concentric pattern attains the maximum value for UTS, followed by the honeycomb, rectilinear, grid, and triangular patterns. The concentric pattern achieved the highest strength because the layers were in a straight line of subjected tensile load. This is believed to help the load spread out evenly (uniformly distributed across the concentric pattern), resulting in higher strength values.

3.1.3 Yield strength (0.2% offset)

The yield strength of a material is a fixed value representing its ultimate elasticity. The yield strength is the stress at which a material changes from elastic to plastic. When a material is stressed below its yield point, it deforms elastically, bouncing back to its original shape when the tension is released. Figure 7 displays that a concentric infill pattern with 75% infill density produced a maximum yield strength

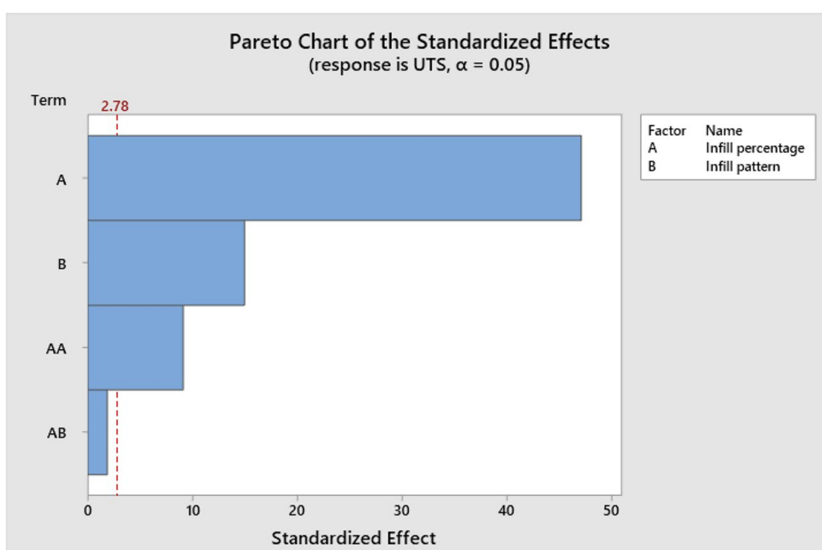

Fig. 11 Pareto chart of UTS

Table 6 Regression equation of UTS with various infill patterns and infill percentages

Infill pattern	Regression equation
Concentric	10.320 + 0.423 Infill % − 0.003 Infill %*Infill %
Grid	9.577 + 0.414 Infill % − 0.003 Infill %*Infill %
Honeycomb	9.213 + 0.417 Infill % − 0.003 Infill %*Infill %
Rectilinear	8.023 + 0.429 Infill % − 0.003 Infill %*Infill %
Triangle	6.307 + 0.389 Infill % − 0.003 Infill %*Infill %

of 20.00 MPa, and the triangle infill pattern with 25% infill density produced a minimum value of 7.64 MPa. Based on this, the highest suitable properties were obtained at 75% infill, whereas the lowest properties were obtained at 25% infill. This demonstrates that the density of the infill material is another crucial factor in improving the mechanical characteristics of the specimen.

3.2 Compressive properties

The ability of a given specimen or structural element to withstand loads that cause a size reduction is referred to as the material's or element's compressive strength. In this test, the test sample is subjected to a force applied to its top and bottom, and this force continues until the test sample fractures or distorts. Table 4 shows the average compressive properties achieved by the PETG with various infill patterns and infill densities.

3.2.1 Compressive strength

In contrast to the UTS, Fig. 8 reveals that the triangle infill pattern with 75% infill density obtained the highest compressive strength at 24.03 MPa, while the concentric pattern with 25% infill density obtained the lowest strength at 8.15 MPa. Thus, it can be summarized that the strength is highest at 75% infill and lowest at 25% infill density. Regarding pattern, the triangle pattern still achieved the highest strength than the other patterns. The cross-section of the triangle pattern observed could withstand more load than the different patterns, resulting in higher strength at 24.03 MPa.

3.2.2 Compressive modulus

The compression modulus is a measure of a material's stiffness or its resistance to length changes caused by compression. When measuring material rigidity, a higher compression modulus is preferred. Figure 9 states that the maximum modulus value obtained was 3.71 GPa by the

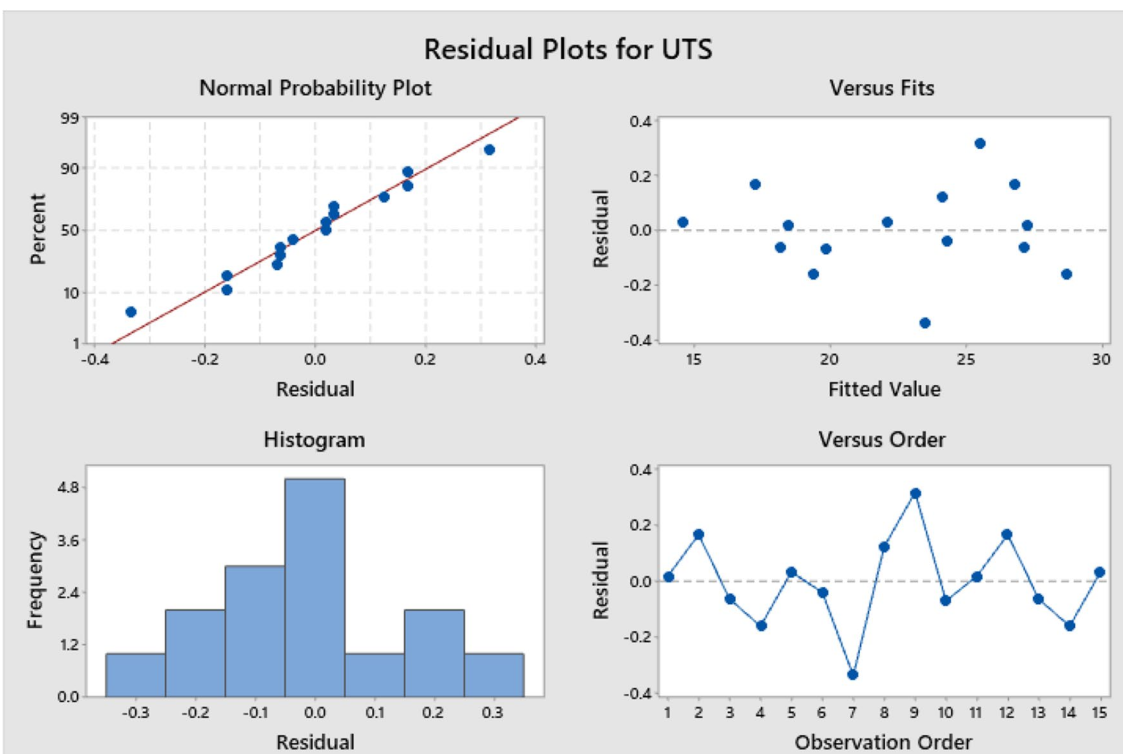

Fig. 12 Residual plots for UTS

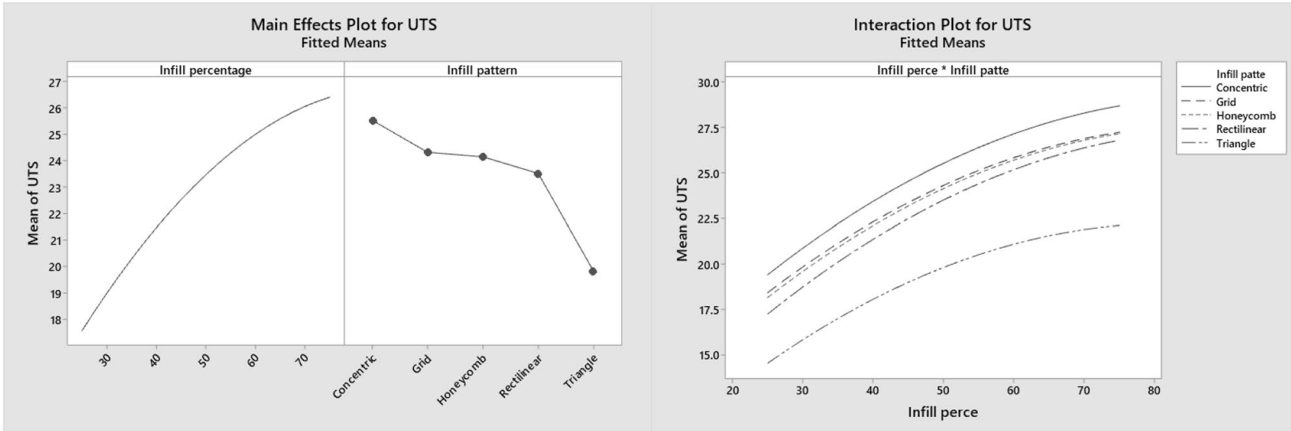

Fig. 13 Effects of infill patterns and infill percentage on UTS

Table 7 Analysis of variance of *E*

Source	DF	Contribution	Adj SS	Adj MS	*F* value	*P* value
Model	10	99.89%	0.387273	0.038727	368.83	0.000
Linear	5	97.27%	0.377120	0.075424	718.32	0.000
Infill %	1	89.24%	0.345960	0.345960	3294.86	0.000
Infill pattern	4	8.04%	0.031160	0.007790	74.19	0.001
Square	1	0.06%	0.000213	0.000213	2.03	0.227
Infill %*Infill %	1	0.06%	0.000213	0.000213	2.03	0.227
2-Way interaction	4	2.56%	0.009940	0.002485	23.67	0.005
Infill %*Infill pattern	4	2.56%	0.009940	0.002485	23.67	0.005
Error	4	0.11%	0.000420	0.000105		
Total	14	100.00%				
R^2 = 99.89%						
R^2 adjusted = 99.62%						
R^2 predicted = 97.71%						

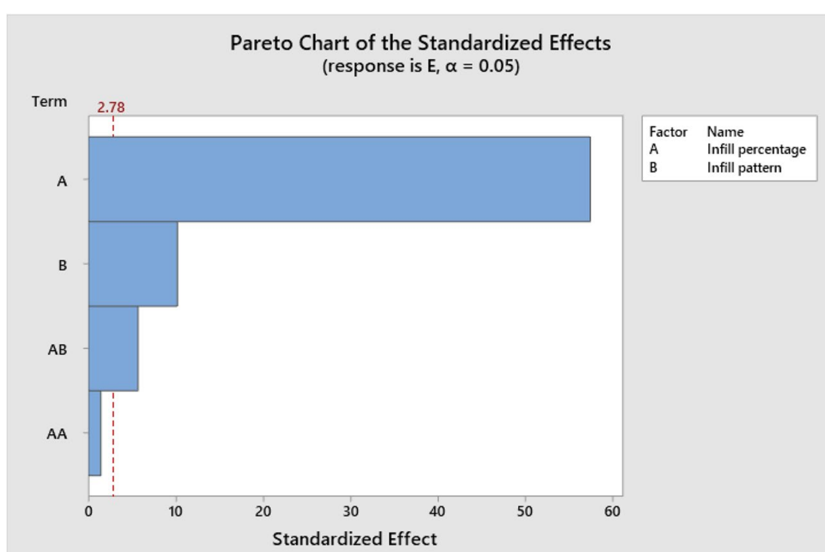

Fig. 14 Pareto chart for *E*

Table 8 Regression equation of E with various infill patterns and infill percentages

Infill pattern	Regression equation
Concentric	0.090 + 0.011 Infill % − 0.001 Infill %*Infill %
Grid	0.150 + 0.008 Infill % − 0.001 Infill %*Infill %
Honeycomb	0.087 + 0.009 Infill % − 0.001 Infill %*Infill %
Rectilinear	0.077 + 0.009 Infill % − 0.001 Infill %*Infill %
Triangle	0.107 + 0.007 Infill % − 0.001 Infill %*Infill %

triangle infill pattern with 75% of infill density, and the lowest value of 0.89 GPa was obtained at the 25 % infill density of the concentric infill pattern. The highest modulus value for grid, honeycomb, rectilinear, and concentric patterns is 3.54, 3.51, 3.49, and 2.74 MPa, respectively.

Figure 10 shows the microstructure image of the tensile and compression samples. Figure 10a shows the microvoids and smooth regions in the air gap. From the figure, it can be concluded that the operating parameters are suitable for this printing process as the microvoids are minimal and have very good smooth bondings within the layers. Figure 10b shows the tensile fractured concentric infill pattern with 50% infill density. The image confirms that for the tensile properties, the load acts uniformly on the pattern, which helps to obtain more strength for the sample to fracture. Figure 10c shows the compressive force-tested samples of concentric patterns with an infill density of 50%. When the compression force is applied to the specimen, the concentric pattern observed not be able to withstand high energy because of the pattern design. Also, from Fig. 10d, the interlayer bonding of the concentric pattern was found not to be in perfect condition, and the voids that occurred during the printing process were seen clearly when compared with the tensile specimens. Thus, it can be concluded that the concentric pattern results in good tensile properties but not for the compressive load.

3.3 Statistical analysis of the tensile properties using RSM

3.3.1 Statistical analysis of ultimate tensile strength

Using RSM, a quadratic regression model of ultimate tensile strength (UTS) as a function of the process parameters of infill density and infill pattern is constructed. Table 5 shows the contribution, standard errors, and the P value obtained. All response characteristics were analyzed by ANOVA. Factors are considered to be statistically significant if their P values (alpha values) are less than 0.05 and to be statistically insignificant if they are greater than 0.05. According to the variance analysis,

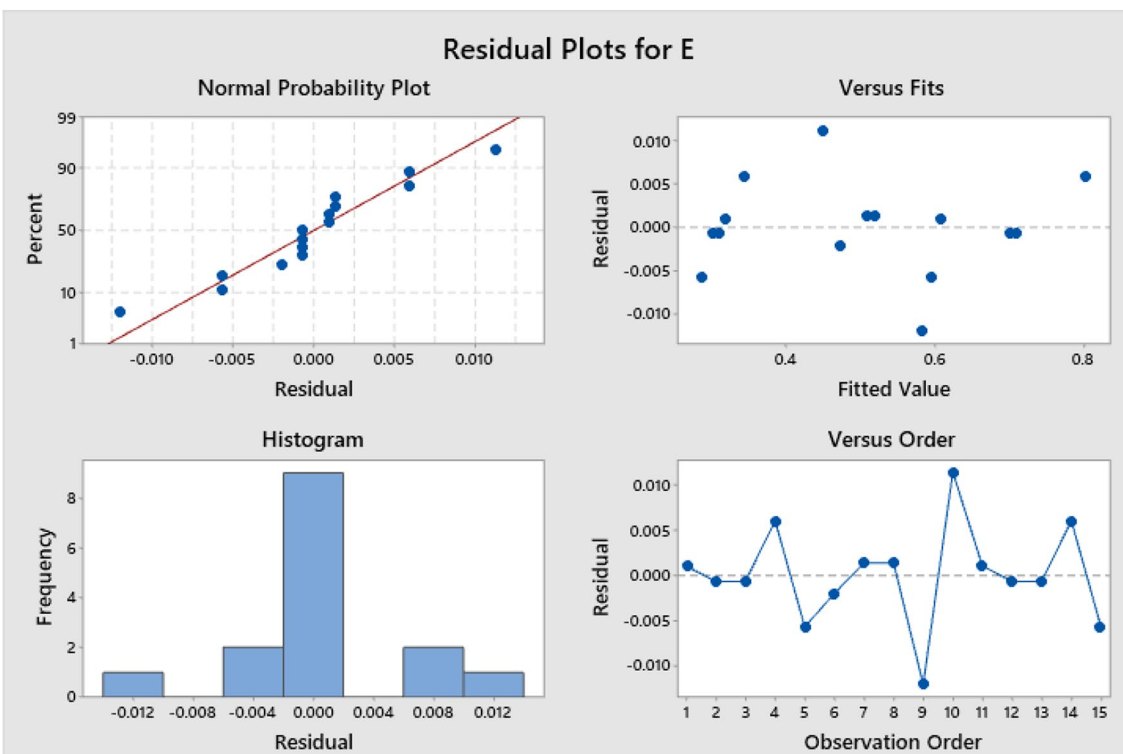

Fig. 15 Residual plots of E

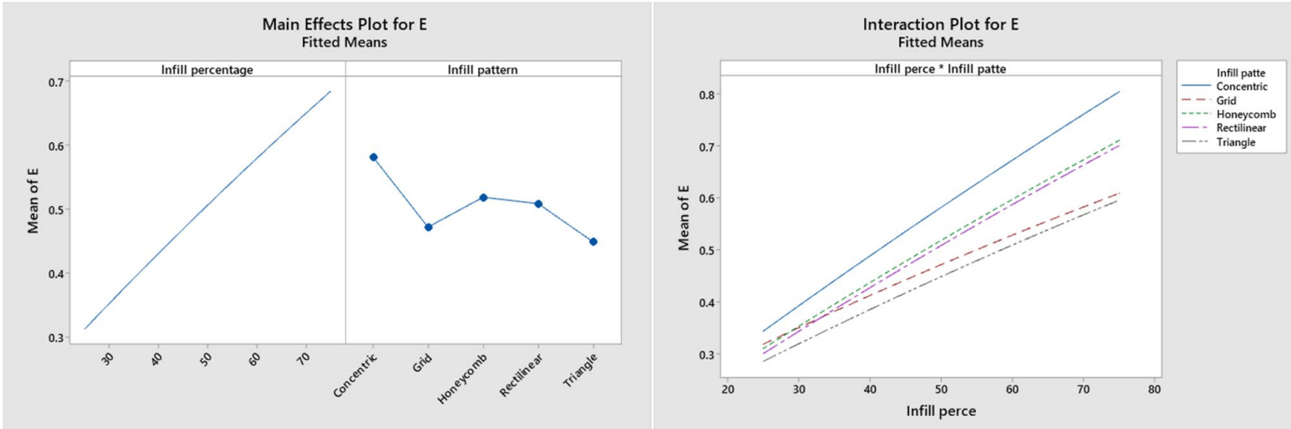

Fig. 16 Effects of infill patterns and infill percentage on *E*

Table 9 Analysis of variance of yield strength

Source	DF	Contribution	Adj SS	Adj MS	*F* value	*P* value
Model	10	99.52%	238.581	23.858	83.03	0.000
Linear	5	99.33%	238.136	47.627	165.76	0.000
Infill %	1	87.96%	210.865	210.865	733.88	0.000
Infill pattern	4	11.38%	27.271	6.818	23.73	0.005
Square	1	0.06%	0.156	0.156	0.54	0.503
Infill %*Infill %	1	0.06%	0.156	0.156	0.54	0.503
2-Way interaction	4	0.12%	0.290	0.073	0.25	0.894
Infill %*Infill pattern	4	0.12%	0.290	0.073	0.25	0.894
Error	4	0.48%	1.149	0.287		
Total	14	100.00%				
$R^2 = 99.52\%$						
R^2 adjusted = 98.32%						
R^2 predicted = 92.89%						

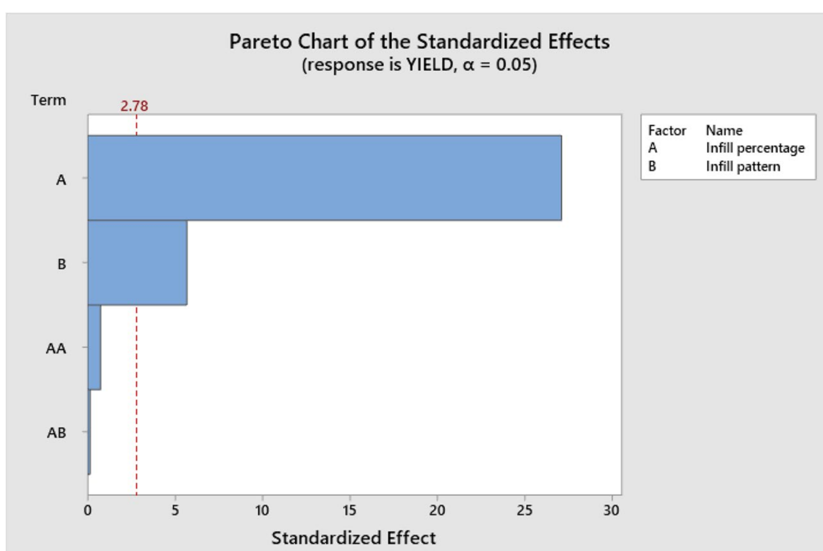

Fig. 17 Pareto chart for yield strength

Table 10 Regression equation of yield strength with various infill patterns and infill percentages

Infill pattern	Regression equation
Concentric	6.930 + 0.205 Infill % – 0.001 Infill %*Infill %
Grid	5.330 + 0.221 Infill % – 0.001 Infill %*Infill %
Honeycomb	5.170 + 0.219 Infill % – 0.001 Infill %*Infill %
Rectilinear	4.610 + 0.223 Infill % – 0.001 Infill %*Infill %
Triangle	2.100 + 0.222 Infill % – 0.001 Infill %*Infill %

when considering each individual's effects, the chosen FDM parameters are found to be significant. From Table 5, the *P* value of the model, infill pattern, and infill density is less than 0.05, concluding that all the factors are significant. More importantly, the infill percentage is the most influential factor compared to the infill pattern. It shows that the interaction of the infill percentage is 75.02%, and the infill pattern is 21.59%. The R^2 value is stated as 99.86%, which demonstrates the statistical measure of fit that reveals how much variance in the dependent variable can be attributed to the independent variable(s) in a regression model. The R^2 adjusted and R^2 predicted values are 99.53% and 97.14%, respectively, acceptable and fitting the data.

Figure 11 shows the Pareto chart of the standardized effect on the infill pattern and infill percentage. It shows that the infill percentage contributes more effects than the infill pattern. Table 6 shows the regression equations of UTS specific to the various factors and can be effective for the prediction of the UTS value. Figure 12 demonstrates the residual plots of UTS. The predicted lines are near the normal line, showing that this model prediction fits with minimal error. Figure 13 shows the main effect plot and the interaction plot of UTS with respect to the various factors. These plots show the impact of the factors in each variable.

3.3.2 Statistical analysis of elastic modulus

Based on the data in Table 7, it can conclude that the model, infill pattern, and infill density are all significant. In addition, when comparing the infill pattern to the infill percentage, the latter factor is less essential. The results demonstrate a correlation between the infill percentage being 89.24% and the infill pattern being 8.04%. In a regression analysis, the proportion of explained variation in the dependent variable that can be assigned to the independent variables is shown by the R^2 value, which is reported as 99.89%. The adjusted R^2

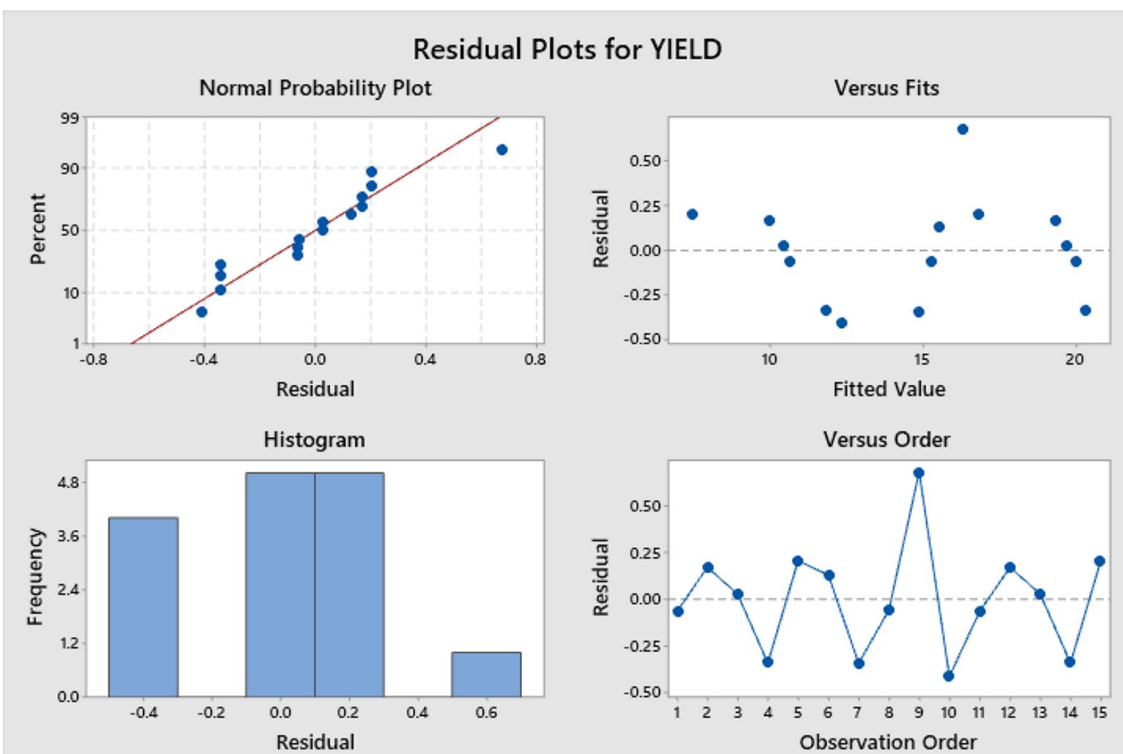

Fig. 18 Residual plots for yield strength

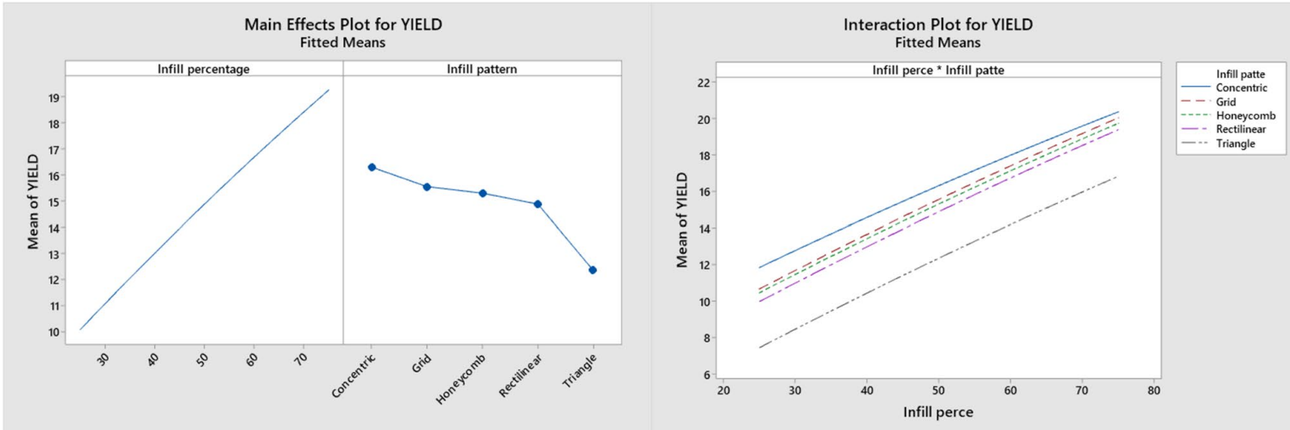

Fig. 19 Effects of infill patterns and infill percentage on yield strength

Table 11 Analysis of variance of CS

Source	DF	Contribution	Adj SS	Adj MS	*F* value	*P* value
Model	10	99.89%	355.475	35.548	361.67	0.000
Linear	5	99.62%	354.508	70.902	721.38	0.000
Infill %	1	89.54%	318.660	318.660	3242.15	0.000
Infill pattern	4	10.07%	35.848	8.962	91.18	0.000
Square	1	0.08%	0.298	0.298	3.03	0.157
Infill %*Infill %	1	0.08%	0.298	0.298	3.03	0.157
2-Way interaction	4	0.19%	0.669	0.167	1.70	0.309
Infill %*Infill pattern	4	0.19%	0.669	0.167	1.70	0.309
Error	4	0.11%	0.393	0.098		
Total	14	100.00%				
$R^2 = 99.89\%$						
R^2 adjusted = 99.61%						
R^2 predicted = 97.67%						

Fig. 20 Pareto chart for CS

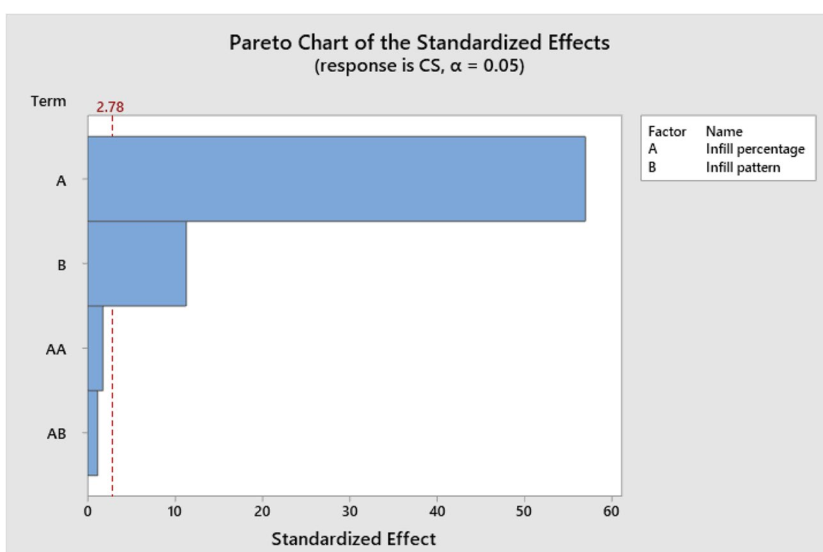

Table 12 Regression equation of CS with various infill patterns and infill percentages

Infill pattern	Regression equation
Concentric	1.737 + 0.264 Infill % − 0.005 Infill %*Infill %
Grid	5.313 + 0.259 Infill % − 0.005 Infill %*Infill %
Honeycomb	3.887 + 0.284 Infill % − 0.005 Infill %*Infill %
Rectilinear	3.763 + 0.284 Infill % − 0.005 Infill %*Infill %
Triangle	5.820 + 0.277 Infill % − 0.005 Infill %*Infill %

value is 99.62%, and the predicted R^2 is 97.71%, which are satisfactory and in line with the data for the modulus.

The standard influence on the infill percentage and pattern is depicted in a Pareto chart in Fig. 14. These results demonstrate that the infill percentage has a more significant impact than the infill pattern itself. Table 8 displays the regression equations for the elastic modulus that are factor-specific and can be used to estimate *E* values accurately. As seen in Fig. 15, which depicts residual plots for the modulus, the predicted lines are extremely close to the normal line, indicating that this model prediction could predict the data with minimal error. The impact of each factor on each variable is depicted in Fig. 16's main effect plot and interaction plot of elastic modulus with respect to the various components.

3.3.3 Statistical analysis of yield strength (0.2% offset)

From Table 9, the *P* value of the model, infill pattern, and infill density is less than 0.05. It shows that all the factors are significant. More importantly, the infill percentage is the most influential factor compared to the infill pattern. The infill percentage's interaction is 87.96%, and the infill pattern is 11.38%. The R^2 value obtained is 99.52% demonstrating the statistical measure of fit that reveals how much variance in the dependent variable can be attributed to the independent variable(s) in a regression model. The R^2 adjusted and R^2 predicted values are 98.32% and 92.89%, respectively, acceptable and fitting the data.

Figure 17 shows the Pareto chart of the standardized effect on the infill pattern and infill percentage. It shows that the infill percentage contributes more effects than the infill pattern. Table 10 shows the regression equations of yield strength specific to the various factors, which can be effective for predicting the yield strength value. Figure 18 demonstrates the residual plots of yield strength. The predicted lines are near the normal line, showing that this model prediction could estimate the properties with minimal error. Figure 19 shows the main effect plot and the interaction plot of yield strength with respect to the various factors, and these plots show the impact of the factors in each variable.

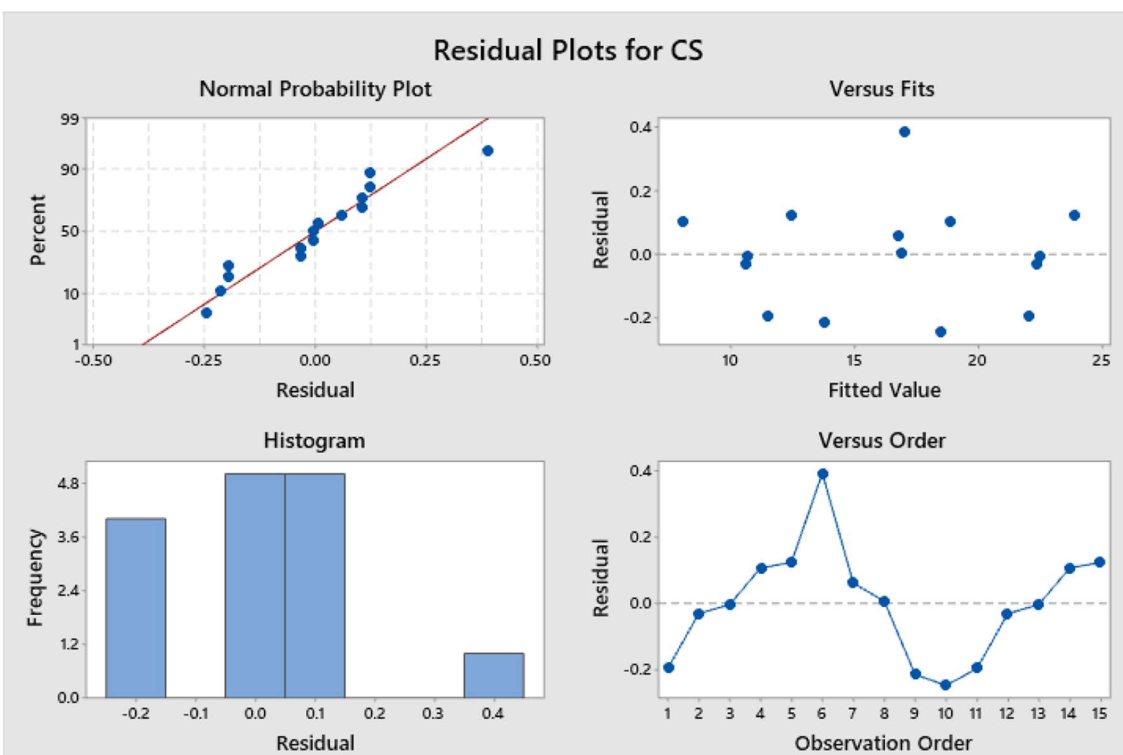

Fig. 21 Residual plots for CS

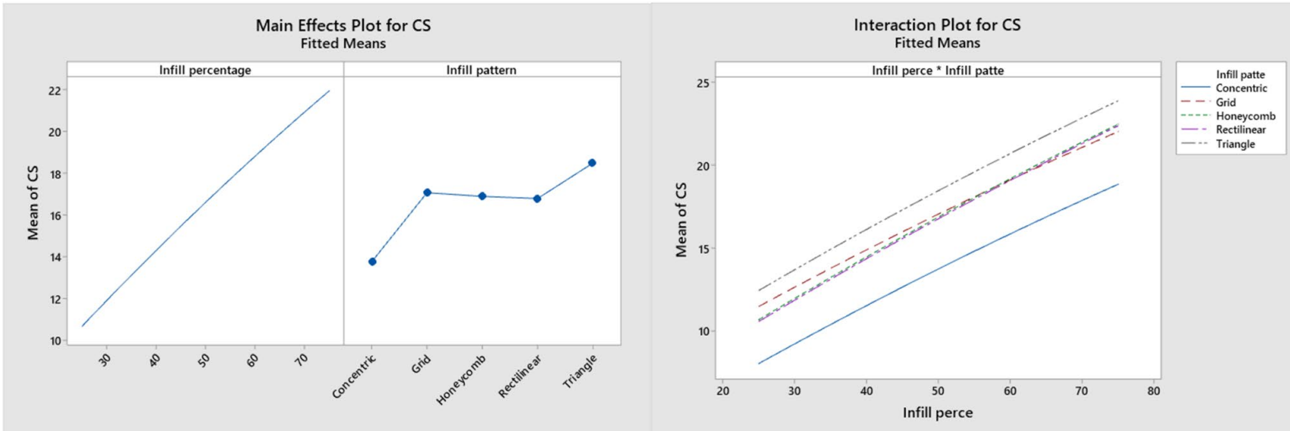

Fig. 22 Regression equation of CS with various infill patterns and infill percentages

Table 13 Analysis of variance of CM

Source	DF	Contribution	Adj SS	Adj MS	*F* value	*P* value
Model	10	98.75%	12.0503	1.20503	31.62	0.002
Linear	5	98.26%	11.9902	2.39804	62.92	0.001
Infill %	1	81.62%	9.9600	9.96004	261.34	0.000
Infill pattern	4	16.64%	2.0302	0.50754	13.32	0.014
Square	1	0.37%	0.0449	0.04485	1.18	0.339
Infill %*Infill %	1	0.37%	0.0449	0.04485	1.18	0.339
2-Way interaction	4	0.13%	0.0153	0.00382	0.10	0.977
Infill %*Infill pattern	4	0.13%	0.0153	0.00382	0.10	0.977
Error	4	1.25%	0.1524	0.03811		
Total	14	100.00%				
R^2 = 98.75%						
R^2 adjusted = 95.63%						
R^2 predicted = 91.65%						

Fig. 23 Pareto chart for CM

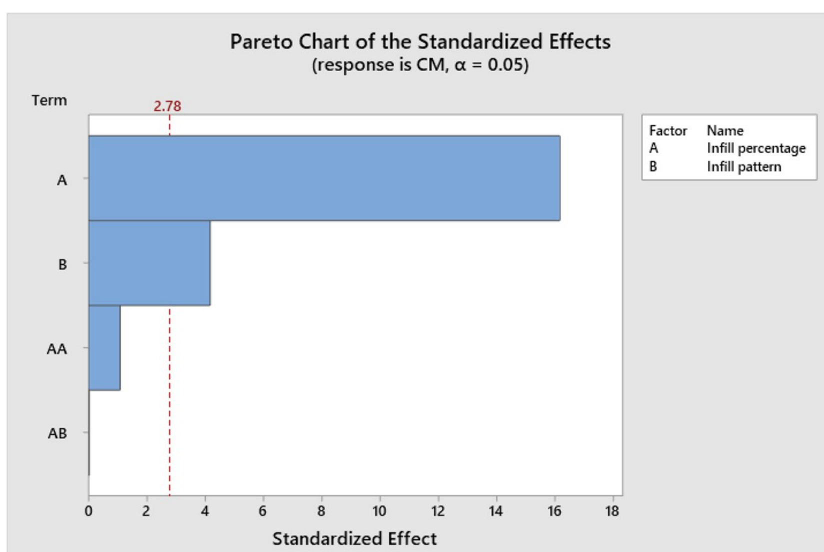

Table 14 Regression equation of CM with various infill patterns and infill percentages

Infill pattern	Regression equation
Concentric	−0.513 + 0.056 Infill % − 0.002 Infill %*Infill %
Grid	0.270 + 0.059 Infill % − 0.002 Infill %*Infill %
Honeycomb	0.163 + 0.059 Infill % − 0.002 Infill %*Infill %
Rectilinear	0.073 + 0.059 Infill % − 0.002 Infill %*Infill %
Triangle	0.287 + 0.060 Infill % − 0.002 Infill %*Infill %

3.4 Statistical analysis of the compressive properties using RSM

3.4.1 Statistical analysis of the compressive strength

Based on the data in Table 11, it can be concluded that the model, infill pattern, and infill density are all significant. In addition, when comparing the infill pattern to the infill percentage, the latter factor is less essential. The results demonstrate a correlation between the infill percentage is 89.54% and the infill pattern is 10.07%. In a regression analysis, the proportion of explained variation in the dependent variable that can be assigned to the independent variables is shown by the R^2 value, which is reported as 99.89%. The adjusted R^2 value is 99.61%, and the predicted R^2 is 97.67%, which are satisfactory and in line with the data for the modulus.

The standard influence on the infill percentage and pattern is depicted in a Pareto chart in Fig. 20. These results demonstrate that the infill percentage has a more significant impact than the infill pattern. Table 12 displays the factor-specific regression equations for the CS that can be used to estimate CS values accurately. As seen in Fig. 21, which depicts residual plots for the modulus, the predicted lines are extremely close to the normal line, indicating that this model prediction could estimate the properties with minimal error. The impact of each factor on each variable is depicted in Fig. 22's main effect plot and interaction plot of CS with respect to the various components.

3.4.2 Statistical analysis of the compressive modulus

From Table 13, the *P* value of the model, infill pattern, and infill density is less than 0.05. It shows that all the factors are significant. More importantly, the infill percentage is the most influential factor compared with the infill pattern. It shows that the interaction of the infill percentage is 81.62%, and the infill pattern is 16.64%. The R^2 value is stated as 98.75%. It demonstrates the statistical measure of fit that reveals how much variance in the dependent variable can be attributed to the independent variable(s) in a regression model. The R^2 adjusted and R^2 predicted values are 95.63% and 91.65%, respectively, which are acceptable and fit the data.

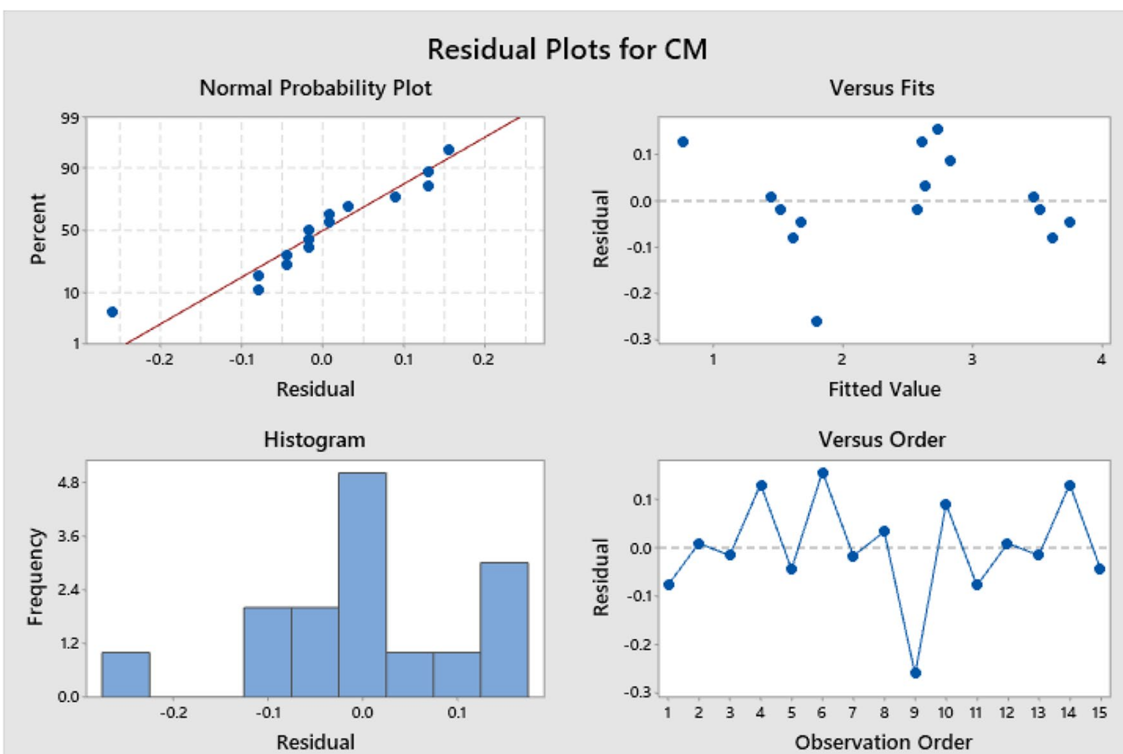

Fig. 24 Residual plots for CM

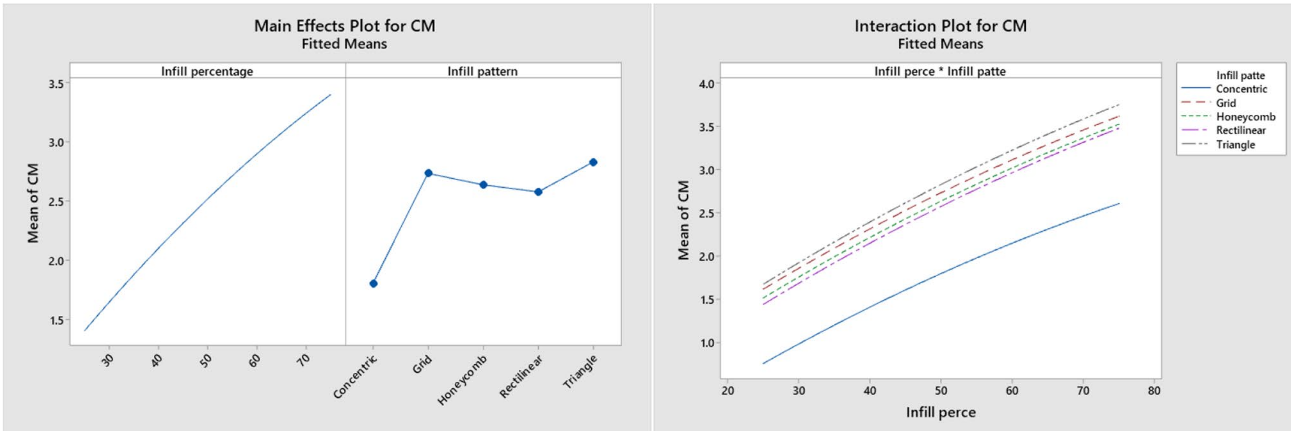

Fig. 25 Regression equation of CM with various infill patterns and infill percentages

Figure 23 shows the Pareto chart of the standardized effect on the infill pattern and infill percentage. It shows that the infill percentage contributes more effects than the infill pattern. Table 14 shows the regression equations of CM specific to the various factors and can be effective for predicting the CM value. Figure 24 demonstrates the residual plots of CM. The predicted lines are near the normal line, showing that this model prediction could estimate the properties with minimal error. Figure 25 shows the main effect plot and the interaction plot of CM with respect to the various factors. These plots show the impact of the factors in each variable.

4 Conclusion

The primary goal of this work is to employ the FDM technique to analyze the tensile and compression properties of PETG printed specimens at different infill patterns and infill percentages. The highest UTS, *E*, and yield values were found to be 28.53 MPa, 0.81 GPa, and 20.00 MPa, respectively, for the 75% infill concentric pattern. The maximum CS and CM values are 24.03 MPa and 3.71 GPa for the triangle pattern with a 75% infill percentage. The regression equation for the enhanced mechanical characteristics of the PETG was developed using the RSM method, and optimization was performed to discover the ideal values for the relevant process parameters.

- Concentric infill pattern is best for tensile loads and not suitable for compression loads because of the layout of the inner structure of the pattern.
- Increasing the infill pattern will enhance the mechanical properties.
- The response surface methodology is a useful tool for effectively planning experiments methodically. It can be concluded with 95% certainty that the mathematical relations constructed between dependent and independent parameters are significant for properties prediction.
- Regression equations can be used to perform numerical analysis, allowing for more informed choice-making in the present and the future.

Acknowledgements The authors gratefully acknowledge the Universiti Malaysia Pahang, Malaysia, for providing funds and facilities under research grant RDU192216 to conduct this research.

Code availability Not applicable.

Author contribution Rajan Kumaresan: data curation, writing—original draft preparation. Mahendran Samykano: supervision, conceptualization. Kumaran Kadirgama: supervision, writing—reviewing and editing. Adarsh Kumar Pandey: reviewing and editing. Md. Mustafizur Rahman: writing—reviewing and editing.

Funding Universiti Malaysia Pahang, Grant RDU192216.

Data availability Data sharing not applicable to this article as no datasets were generated or analyzed during the current study.

Declarations

Ethics approval Not applicable.

Consent to participate Consent to participate has been received from all co-authors before the work is submitted.

Consent for publication Consent to publication has been received from all co-authors before the work is submitted

Competing interests The authors declare no competing interests.

References

1. Ngo TD, Kashani A, Imbalzano G, Nguyen KTQ, Hui D (2018) Additive manufacturing (3D printing): a review of materials,

methods, applications and challenges. Compos B Eng 143:172–196. https://doi.org/10.1016/j.compositesb.2018.02.012
2. Wang X, Jiang M, Zhou Z, Gou J, Hui D, Melocchi A, Parietti F, Loreti G, Maroni A, Gazzaniga A et al (2018) Additive manufacturing techniques in manufacturing -an overview. Mater Today: Proc 3:3873–3882. https://doi.org/10.1016/j.matpr.2017.11.642
3. Rajan K, Samykano M, Kadirgama K, Harun WSW, Rahman MM (2022) Fused deposition modeling: process, materials, parameters, properties, and applications. Int J Adv Manuf Technol 120:1531–1570
4. Ryan KR, Down MP, Banks CE (2021) Future of additive manufacturing: overview of 4D and 3D printed smart and advanced materials and their applications. Chem Eng J 403:126162
5. Guddati S, Kiran ASK, Leavy M, Ramakrishna S (2019) Recent advancements in additive manufacturing technologies for porous material applications. Int J Adv Manuf Technol 105:193–215. https://doi.org/10.1007/s00170-019-04116-z
6. Tofail SAM, Koumoulos EP, Bandyopadhyay A, Bose S, O'Donoghue L, Charitidis C (2018) Additive manufacturing: scientific and technological challenges, market uptake and opportunities. Mater Today 21:22–37
7. Chacón JM, Caminero MA, García-Plaza E, Núñez PJ (2017) Additive manufacturing of PLA structures using fused deposition modelling: effect of process parameters on mechanical properties and their optimal selection. Mater Des 124:143–157. https://doi.org/10.1016/j.matdes.2017.03.065
8. Singh R, Gupta A, Tripathi O, Srivastava S, Singh B, Awasthi A, Rajput SK, Sonia P, Singhal P, Saxena KK (2020) Powder bed fusion process in additive manufacturing: an overview. Mater Today: Proc 26:3058–3070. https://doi.org/10.1016/j.matpr.2020.02.635
9. Selvamani SK, Rajan K, Samykano M, Kumar RR, Kadirgama K, Mohan RV (2022) Investigation of tensile properties of PLA–brass composite using FDM. Prog Addit 7:839–851. https://doi.org/10.1007/s40964-021-00255-6
10. Selvamani SK, Ngui WK, Rajan K, Samykano M, Kumar R, Badadhe AM (2022) Investigation of bending and compression properties on PLA-brass composite using FDM. Phys Chem Earth, Parts A, B, C 128:103251. https://doi.org/10.1016/j.pce.2022.103251
11. Kumaresan R, Samykano M, Kadirgama K, Ramasamy D, Keng NW, Pandey AK (2021) 3D printing technology for thermal application: a brief review. J Adv Res Fluid Mech Therm Sci 83:84–97. https://doi.org/10.37934/ARFMTS.83.2.8497
12. Daminabo SC, Goel S, Grammatikos SA, Nezhad HY, Thakur VK (2020) Fused deposition modeling-based additive manufacturing (3D printing): techniques for polymer material systems. Mater Today Chem 16:100248. https://doi.org/10.1016/j.mtchem.2020.100248
13. Özen A, Abali BE, Völlmecke C, Gerstel J, Auhl D (2021) Exploring the role of manufacturing parameters on microstructure and mechanical properties in fused deposition modeling (FDM) using PETG. Appl Compos Mater 28:1799–1828. https://doi.org/10.1007/s10443-021-09940-9
14. Liu Z, Lei Q, Xing S (2019) Mechanical characteristics of wood, ceramic, metal and carbon fiber-based PLA composites fabricated by FDM. J Mater Res Technol 8:3743–3753. https://doi.org/10.1016/j.jmrt.2019.06.034
15. Dey A, Yodo N (2019) A systematic survey of FDM process parameter optimization and their influence on part characteristics. J Manuf Mater Process 3:64. https://doi.org/10.3390/jmmp3030064
16. Li P, Gong Y, Xu Y, Qi Y, Sun Y, Zhang H (2019) Inconel-steel functionally bimetal materials by hybrid directed energy deposition and thermal milling: microstructure and mechanical properties. Arch Civ Mech 19:820–831. https://doi.org/10.1016/j.acme.2019.03.002
17. Peng X, Kuang X, Roach DJ, Wang Y, Hamel CM, Lu C, Qi HJ (2021) Integrating digital light processing with direct ink writing for hybrid 3D printing of functional structures and devices. Addit Manuf 40:101911. https://doi.org/10.1016/j.addma.2021.101911
18. Hanon MM, Marczis R, Zsidai L (2019) Anisotropy evaluation of different raster directions, spatial orientations, and fill percentage of 3D printed PETG tensile test specimens. Key Eng Mater 821:167–173. https://doi.org/10.4028/www.scientific.net/KEM.821.167
19. Szykiedans K, Credo W, Osiński D (2017) Selected mechanical properties of PETG 3-D prints. Procedia Eng 177:455–461
20. Bhandari S, Lopez-Anido RA, Gardner DJ (2019) Enhancing the interlayer tensile strength of 3D printed short carbon fiber reinforced PETG and PLA composites via annealing. Addit Manuf 30:100922
21. Guessasma S, Belhabib S, Nouri H (2019) Printability and tensile performance of 3D printed polyethylene terephthalate glycol using fused deposition modelling. Polymers 11:1220. https://doi.org/10.3390/polym11071220
22. Srinivasan R, Nirmal Kumar K, Jenish Ibrahim A, Anandu KV, Gurudhevan R (2020) Impact of fused deposition process parameter (infill pattern) on the strength of PETG part. Mater Today: Proc 27:1801–1805
23. Barrios JM, Romero PE (2019) Improvement of surface roughness and hydrophobicity in PETG parts manufactured via fused deposition modeling (FDM): an application in 3D printed self-cleaning parts. Materials 12:2499. https://doi.org/10.3390/ma12152499
24. Hsueh MH, Lai CJ, Wang SH, Zeng YS, Hsieh CH, Pan CY, Huang WC (2021) Effect of printing parameters on the thermal and mechanical properties of 3D-printed PLA and PETG, using fused deposition modeling. Polymers 13:1758. https://doi.org/10.3390/polym13111758

Publisher's note Springer Nature remains neutral with regard to jurisdictional claims in published maps and institutional affiliations.

Springer Nature or its licensor (e.g. a society or other partner) holds exclusive rights to this article under a publishing agreement with the author(s) or other rightsholder(s); author self-archiving of the accepted manuscript version of this article is solely governed by the terms of such publishing agreement and applicable law.